A robust finite element-based filter for digital image and volume correlation displacement data

Thorsten Hermann Becker[1*], *Thomas James Marrow*[2]

[1] Department of Mechanical and Mechatronic Engineering, Joubert street, Mechanical Engineering building, Stellenbosch University, Stellenbosch, 7600, South Africa. Email: tbecker@sun.ac.za. Tel.: +27 21 8084045

[2] Department of Materials, University of Oxford, Parks Road, Oxford, OX1 3PH, United Kingdom. Email: james.marrow@materials.ox.ac.uk. Tel.: +44 1865 273938

Abstract

Background: Digital Image and Volume Correlation (DIC and DVC) are non-contact measurement techniques that are used during mechanical testing for quantitative mapping of full-field displacements. The relatively high noise floor of DIC and DVC, which is exasperated when differentiated to obtain strain fields, often requires some form of filtering. Techniques such as median filters or least-squares fitting perform poorly over high displacement gradients, such as the strain localisation near a crack tip, discontinuities across crack flanks or large pores. As such, filtering does not always effectively remove outliers in the displacement field.

Objective: This work proposes a robust finite element-based filter that detects and replaces outliers in the displacement data using a finite element method-based approximation.

Methods: A method is formulated for surface (2D and Stereo DIC) and volumetric (DVC) measurements. Its validity is demonstrated using analytical and experimental displacement data around cracks, obtained from surface and full volume measurements.

Results: It is shown that the displacement data can be filtered in such a way that outliers are identified and replaced. Moreover, data can be smoothed whilst maintaining the nature of the underlying displacement field such as steep displacement gradients or discontinuities.

Conclusions: The method can be used as a post-processing tool for DIC and DVC data and will support the use of the finite element method as an experimental-numerical technique.

Keywords

digital image correlation, digital volume correlation, filter, finite element method, fracture mechanics

---

[*] Corresponding author.

Abbreviations and Symbols

BC	Boundary condition
DIC	Digital image correlation
DVC	Digital volume correlation
FE	Finite Element
MAD	median absolute deviation
ROI	Region of interest
θ	Median of $\lvert \boldsymbol{f}_n \rvert$
Ω	FE domain
α	Yield offset
σ_o	Yield strength
ρ	Density
ρ_l	Elemental density, $\in [0,1]$
$C1, C2, C3$	Convergence criteria 1, 2 and 3.
E	Young's modulus
E_l	Elemental Young's modulus
E_{min}	nominal Young's modulus of the masked region
E_0	nominal Young's modulus of the material
e	Essential boundary condition
$\boldsymbol{f}$	Force vectors
$\boldsymbol{f}_n$	Displacement resultant force vectors
$\boldsymbol{f}_e$	Replacement force vectors, $\in [0]$
$\boldsymbol{K}$	Stiffness matrix
$\boldsymbol{K}_l$	Element stiffness matrix
$\boldsymbol{K}_l^0$	Element stiffness matrix with nominal Young's modulus of the material
m	Hardening coefficient
n	Neutral boundary condition
$\boldsymbol{u}$	Displacement vectors
$\boldsymbol{u}_n$	Measured displacement vectors
$\boldsymbol{u}_e$	Replacement displacement vectors
v	Poisson's ratio
$\boldsymbol{x}$	Cartesian coordinate system

1 Introduction

Full-field displacement measurements are widely used in the field of solid mechanics, both as a surface [1, 2] and as a volume measurement [3–5]. When strain fields are required, there are several techniques which enable their extraction directly, such as laser interferometry (or the grid method) [6], and in crystalline materials, the surface [7] and volumetric [8] strains can be obtained from analysis of diffraction. However, with Digital Image Correlation (DIC) and Digital Volume Correlation (DVC), the strains are not directly available from the experimental technique. This necessitates differentiation of the displacement data, typically using finite differences approaches. However, the differentiation of potentially noisy displacement fields can amplify the subsequent mechanical analysis errors that depend on the displacement gradients and strains [9].

A long-standing solution is to smooth displacement data before numerical differentiation, for example, using mean or median filters [10] or low band pass filters [11, 12]. Alternatively, local least-squares matching to a specified region is used to provide analytical derivatives for the fitting function, such as a lower-order polynomial [10]. Such approaches may be tuned with the classical tools, such as weighted least squares or multiple-cross validation. The challenge in these approaches lies in selecting the specified region and appropriate polynomial order. Often difficulties arise close to strain localisations such as a crack tip and near discontinuities such as crack flanks or specimen edges, leading to non-physical displacement derivatives and hence strain data. Another alternative method is through the finite element (FE) framework [13–16]. These approaches minimise displacement noise by enforcing piece-wise continuity between the element shape functions. The subsequent strains can then be calculated through the FE displacement-strain relationship. However, outliers can still result in measurement, due to various reason such as poor correlation in the input displacements. [14, 17].

This work proposes an alternate FE-based filter to identify and replace displacement outliers from full-field displacement data. The method uses internal reaction forces as an error estimator, whereby data is assessed posteriori using the principle of conservation of energy. Similar works have been applied using variational principles [18–20]; however, this work focuses on outliers that are distinct from random error by locally removing bias errors. An iterative procedure is developed with a convergence criterion to ensure that the outlier removal effect on the underlying data (and remaining random errors) is minimal, i.e. to preserve observed material behaviour. The FE-based procedure is the density-based homogenisation

approach [21], often used for efficient topology optimisation as proposed by Bendsøe [22]. The method is optimised for efficiency to allow for an iterative procedure and is written in MATLAB. Much of the efficiency derives from the use of linear-elastic elements and regular Cartesian grids, amenable due to most DIC and DVC methods using low order subsets and regular grids for similar computational efficiency reasons.

The concept of employing an FE-based framework for data manipulation is not new. For example, Hegland et al. [23] proposed the use of FE thin-plate splines as a surface fitting and smoothing tool. Similarly, the work by Yoneyama et al. [14, 15], Garcia [24] and Becker et al. [16] proposed an FE-based framework for the analysis of surface displacement data obtained using Digital Image Correlation. The approach is not a replacement to current least squares strategies or FE-based strategies but proposes a method that can be applied when spurious signals are too subtle or complex to filter using these methods.

The paper has applied the proposed FE-based method to artificially generated displacement data for validation, and also to experimental Stereo-DIC and volumetric DVC data to demonstrate its implementation. In particular, the paper uses cracked specimens to demonstrates its versatility. This provides perspectives on the numerical effort involved in FE-based outlier removal strategies.

2 Identification of non-physical displacement data

Displacement measurement uncertainty is divided into two types of error, namely variance and bias [25]. Variance refers to a random error, typically normally distributed with the mean representing the true value, and bias refers to an offset error that shifts the mean value from the true value. While the variance is representative of the measurement noise in the system, for example, from image sensor noise or subset matching, bias occurs from factors that include smoothing, poor calibration, or out of plane motion in the case of 2D-DIC. Ideally, bias is removed from the measurement in the analysis to achieve better accuracy. Variance, on the other hand, is an indicator in the precision of the experimental measurement system.

To quantify these types of error, the International Digital Image Correlation Society (iDICs) [25] recommends undertaking some form of rigid body test that is representative of the planned testing activity, where the rigid body displacement is precisely known. The result is used to find a compromise between bias and variance by adjusting the experimental and system setup.

However, since the sources of bias and variance are often related to the underlying deformation field (such as a strain-localisation), a rigid body test may not be representative of the underlying test, and it is challenging to quantify variance and bias in the measurements accurately.

One way to overcome this is to assume an underlying solution. The FE method presents a convenient way by imposing its requirements, i.e., conservation of energy, to the measured displacement field. The solid mechanic's solution to the FE method requires forces to be in equilibrium, a compatible displacement field, and a stress-strain relation that adheres to Hooke's law, for instance. By imposing a FE framework on the measured displacement data and subsequently measuring deviations from the FE prediction, this allows for the representation of both variance and bias. Moreover, the advantage of using a FE framework is that the statistical nature of deviations between measurement and the FE prediction allows us to differentiate between variance and bias. This is detailed below.

2.1 Finite element framework

Consider a full-field experiment of a cracked specimen loaded in tension, as illustrated in Figure 1 (a). Displacement data is captured with either surface or volume imaging before and after loading, as illustrated in Figure 1 (b). The full-field displacement map is obtained between the reference and deformed image with the use of a correlation algorithm, such as 2D-DIC (single camera system to capture only in-plane displacements), Stereo-DIC (multiple camera system to capture both in-plane and out-of-plan displacements) or DVC (using, for example, X-ray tomography to capture the full three-dimensional displacements). This usually involves dividing the reference image into groups of pixels called subsets (or subvolumes of voxels in DVC), where relative displacements are determined per subset by matching the optimal location between the reference and the deformed image (or vice-versa). A region of interest (ROI) can be selected, whereby a mask is defined in which the displacement map is computed (the mask excludes data points from the correlation process outside the ROI).

Potential sources of a measurement bias are illustrated in Figure 1 (b). The illustration shows a crack or discontinuity representing a geometric feature resulting in subset smearing, and an artefact representing, for example, a foreign body (e.g. surface contamination between observations) resulting in low subset correlation. While not explicitly illustrated, other sources of error may include some form of calibration, amongst others [10, 25–27].

The displacement field $\boldsymbol{u}$ is computed within the ROI, as shown in Figure 1 (b). In the illustration, regions near the discontinuity and artefact are erroneous and have been labelled as outliers. Typically, in such a problem, some form of filter[†] is applied to identify and potentially replace outliers. However, this approach often fails at the discontinuity or may ignore larger regions of outliers (limited by the moving window size). Alternatively, the nodal force values $\boldsymbol{f}$ can be computed by imposing $\boldsymbol{u}$ as a boundary condition to a FE problem over its domain, Ω, as shown in Figure 1 (c). If the condition of conservation of energy is met, internal force vectors should be negligible. Force outliers are a consequence of non-physical displacement outliers.

The advantage of considering outliers in $\boldsymbol{f}$, rather than $\boldsymbol{u}$, lies in that a *valid* displacement value has a zero-force value; the variance is manifested in $\boldsymbol{f}$'s distribution and bias as a shift from a zero-mean value. Moreover, since outliers are identified based on the statistical nature in $\boldsymbol{f}$, elastic properties of the material being testing are not required, as later shown.

The FE-based framework uses the efficient approach presented by Liu and Tovar [28], developed initially by Bendsøoe [22], in that a regularly spaced and gridded array of data points is considered. This means that shape function derivatives and their respective Jacobian need only be computed once. The use of a gridded approach is motivated by several factors: (i) the relatively noisy nature of DIC and DVC coupled with the inherent subset smearing does not warrant non-regular FE implementation complexities that allow for mesh refinement; (ii) DIC and DVC typically use a gridded approach in positioning subsets; and (iii) it allows for direct implementation from the computed displacement field into the FE domain without requiring knowledge of the specimen geometry nor requiring some form of interpolation approach when mapping displacement from the measurement to the FE domain.

Liu and Tovar comprehensively cover the implementation of the FE framework and, therefore, only the relevant overview and specific alterations are presented. Briefly, the method draws the material stiffness distribution as elemental densities, ρ_l, from the spatially defined density

[†] Common filters include the mean and median filters that are used in most commercial DIC systems.

grading $\rho(\boldsymbol{x})$, in which $\boldsymbol{x}$ is the global coordinate system. This is used to define an element-specific Young's modulus, E_l, as

$$E_l(\rho_l) = E_{min} + \rho_l(E_0 - E_{min}), \quad \rho_l \in [0,1] \tag{1}$$

In the presented method, ρ_l is set according to the DIC or DVC defined mask, where ρ_l is unity inside and zero outside the mask. E_0 is the nominal Young's modulus of the material and which is set to unity. E_{min} is the nominal Young's modulus of masked material and is set to a near-zero value of $1{\cdot}10^{-10}$. By using this approach, the geometry of the specimen does not need to be accurately modelled but can be directly linked to the already established ROI of the DIC or DVC problem. Masking to consider, for example, a crack can easily be incorporated using crack detection algorithms such as the phase congruency method developed by Cinar *et al.* [29].

The element stiffness matrix, $\boldsymbol{K}_l$, is constructed with generalised Hooke's law, and linear shape functions for a 4-node quadrilateral or 8-node hexagonal element for 2D-DIC or stereo-DIC and DVC respectively, as

$$\boldsymbol{K}_l(E_l(\rho_l), v) = E_l(\rho_l)\boldsymbol{K}_l^0(v) \tag{2}$$

where, $\boldsymbol{K}_l^0$ is the element stiffness matrix with a unit Young's modulus and v is Poisson's ratio, which is set to 0.3. E_l is determined using Eqn. (1). The elemental stiffness matrices are assembled into the global stiffness matrix, $\boldsymbol{K}$, over $\boldsymbol{\Omega}$ defined by the ROI.

$$\boldsymbol{K}(E_l(\rho_l), v)\boldsymbol{u} = \boldsymbol{f} \tag{3}$$

For computational efficiency, $\boldsymbol{K}$ is partitioned into displacement and force constrained quantities, denoted by subscripts n (natural) and e (essential). Thus, the assembled matrix can be rewritten as

$$\begin{bmatrix} \boldsymbol{K}_{ee} & \boldsymbol{K}_{en} \\ \boldsymbol{K}_{ne} & \boldsymbol{K}_{nn} \end{bmatrix} \begin{Bmatrix} \boldsymbol{u}_e \\ \boldsymbol{u}_n \end{Bmatrix} = \begin{Bmatrix} \boldsymbol{f}_e \\ \boldsymbol{f}_n \end{Bmatrix} \tag{4}$$

The nodal forces and displacements can be solved respectively by

$$\boldsymbol{f}_n = [\boldsymbol{K}_{ne}]\{\boldsymbol{u}_e\} + [\boldsymbol{K}_{nn}]\{\boldsymbol{u}_n\} \quad (5)$$

and

$$\boldsymbol{u}_e = [\boldsymbol{K}_{ee}]^{-1}(\{\boldsymbol{f}_e\} - [\boldsymbol{K}_{en}]\{\boldsymbol{u}_n\}) \quad (6)$$

where, $\boldsymbol{u}_n$ and $\boldsymbol{f}_e$ represent the known displacement and force vectors, and similarly, $\boldsymbol{u}_e$ and $\boldsymbol{f}_n$ the unknown displacement and force vectors, respectively. $\boldsymbol{K}_{ee}$, $\boldsymbol{K}_{en}$, $\boldsymbol{K}_{ne}$ and $\boldsymbol{K}_{nn}$ are the corresponding stiffness matrices. In the presented method, $\boldsymbol{u}_n$ is set to the measured displacement field, and $\boldsymbol{f}_n$ represents the respective force vector distribution for outlier detection. $\boldsymbol{f}_e$ is set to zero for outlier replacement.

2.2 Outlier detection

At its core, the proposed method uses Equations (5) and (6) to detect and replace outliers, respectively. Its implementation requires; i) careful considerations of Ω; ii) assigning of boundary conditions; iii) an outlier detection strategy; iv) outlier replacement. The algorithm is summarised in Table 1.

As the main interest is the removal and replacement of outliers, the approach continues with the assumption that boundaries can be selected with sufficient flexibility. First, Ω is padded with a single array of nodes. This will result in the addition of one element in x_i, where for 2D-DIC $i = 1, 2$ and stereo-DIC and DVC $i = 1, 2, 3$. This is done to allow for the detection and replacement of outliers on the boundary of Ω. The padding is done in such a way to preserve the mask at the boundary of Ω. In the case of Stereo-DIC, this means that the problem is converted from plane-stress to a 3D problem. $\boldsymbol{u}_n$ is set to the measured displacement data in Ω. For the padded nodes, $\boldsymbol{f}_e$ is set to zero, which essentially extrapolates boundary displacements to the padded nodes by using Equation (6). $\boldsymbol{u}_e$ is computed using Equation (6), and subsequently $\boldsymbol{f}_n$ is computed using Equation (5).

Outlier detection uses the assumption that $\boldsymbol{f}_n$ is normally (Gaussian) distributed around zero. Outliers are seen as force values that fall outside the assumption. As such, two types of outlier detection strategy are proposed to identify outliers:

1. A median type filter whereby values more than a specified scaled median absolute deviation (MAD) away from the median are considered as outliers. A median filter is seen as robust, as the distribution is assumed to be symmetric (about the median) and therefore attaches equal importance to positive and negative deviations [30]. The severity of the filter can be set by specifying a MAD cut-off value and therefore allows for both outlier detection and replacement as well as data smoothing (by defining a low MAD).

2. A Grubbs test (maximum normalised residual test [31]) to detect outliers. A significance of 5% is assumed.

Other Outlier detection approaches exist, for example, a mean filter allowing the selection of a standard deviation to define outliers. However, these are seen as less robust, in that they identify a large number of outliers and thereby significantly smooth data. The method can be easily amended to include a different outlier detection strategy on the basis that $\boldsymbol{f}_n$ should be symmetrically distributed around zero.

The components of $\boldsymbol{f}_n$, i.e. in x_1, x_2 (and x_3), are considered independently but are treated as a collective. In other words, a force outlier in one direction results in the node being identified as an outlier. Masked regions do not contribute to $\boldsymbol{f}_n$ as their elemental stiffness is near zero. This is illustrated in Figure 2 with reference to Figure 1.

2.3 Iterative procedure for outlier removal

Displacement outliers are identified and replaced by $\boldsymbol{u}_e$ using Equation (6) by setting $\boldsymbol{f}_e$ equal to zero. At its extreme, the outlier removal would result in a boundary value problem, i.e. all nodes in Ω are replaced under the assumption of a linear elastic solution. This is undesirable for several reasons: (i) the method aims to detect and replace outliers and not to necessarily smooth displacement data, (ii) removing large regions of outliers will inherently result in a linear elastic solution which is undesirable as, (iii) the measured material behaviour should be maintained as this may include some form of non-linearity such, for example, plasticity or localised material degradation due to microcracking that may result in softening of the stiffness modulus [32, 33]. By replacing fewer nodes, the FE computed replacement will continue to

capture non-linearities assuming these span over several nodes. Therefore, an iterative approach is adopted, that limits the number of outliers removed per iteration. This way the linear elastic solution that is assumed to replace outliers is limited to a localised region, ideally within captured non-linearities.

The outlier replacement can, therefore, be interpreted as an incremental strategy, whereby each increment iteration, i, replaces k nodes. We note that the subsequent iteration $i+1$ considers all nodes in Ω.

To develop the convergence criterion, the median of the magnitude of $\boldsymbol{f}_n$ is used. We see this as representing a bias in $\boldsymbol{f}_n$.

$$\theta^{(i)} = median(|\boldsymbol{f}_n|)^{(i)} \tag{7}$$

Three convergence criteria are chosen: The first criteria (C1) is a simple threshold in $\theta^{(i)}$ representing that the bias is near zero. This leads to the first convergence criteria:

$$C1\colon \theta^{(i)} \leq lim_{C1} \tag{8}$$

The second criteria (C2) defines convergence as a relative change with respect to the initial bias $\theta^{(0)}$, before outlier removal. This is expressed as:

$$C2\colon (\theta^{(i)} - \theta^{(i-1)})/\theta^{(0)} \leq lim_{C2} \tag{9}$$

Lastly, the number of iterations is limited (C3). This is expressed as:

$$C3\colon i \geq lim_{C3} \tag{10}$$

To enable comparison in upcoming examples, the parameters have been set as $lim_{C1} = 1 \cdot 10^{-10}$, $lim_{C2} = 1 \cdot 10^{-2}$ and $lim_{C3} = 10$. In practice, we find that the Grubbs outlier detector seldomly requires more than one or two iterations. However, for a median filter convergence requires more iterations and the choice in lim_{C2} becomes more apparent and convergence may not occur with C3, resulting in significant data replacement and over-smoothing (i.e. significant data replacement under a linear-elastic assumption).

3 Validation using numerical displacement data

The numerical validation makes use of synthetic displacement data that was generated using an FE computed displacement field. Known errors are imposed so that their effect and the outlier removal algorithm capabilities are quantitatively measured. To best illustrate the outlier removal algorithm, a plane-stress problem representative of a 2D-DIC measurement is used (aiding in the graphical presentation of outlier data). Stereo-DIC and DVC problems have been tested similarly, but are not reported here. Instead, the implementation of the algorithm using Stereo-DIC and DVC experimental displacement data is presented in Section 4.

The validation utilises a model of a single edge notch tensile (SENT) specimen geometry of unit width and height of three units. The specimen is loaded on the upper and lower boundaries by displacement in opposing directions in u_2 and u_1 is set to zero. A unit size ROI is selected with the crack tip orientated at the origin to remove any boundary effects, as shown in Figure 3 (a). The node spacing is such that nodal positions coincide with the assumed DIC subset windows to form a gridded mesh of 101 x 101 nodes, resulting in a nodal spacing 0.01. The computed displacement data is set as the subset DIC displacement field, as shown in Figure 3 (b). To better capture disablement of data near the crack tip, mesh refinement with collapsed quarter points was done in the vicinity of the crack tip to fit into the four elements sounding the crack tip, shown in the inset in Figure 3 (a). Units are in *mm* and *N*, meaning the unit size geometry is representative of a one *mm* specimen. While this is not typical for a laboratory setup, it is noted that DIC is scale-invariant when not considering physical limitations such as the optics of the camera and lens system. By using a unit size geometry, the results can be readily normalised and scaled.

The Abaqus model (Version 6.13) comprised of 11820 quadratic, 8-noded brick elements (CPE8). The validation assumes properties of ferritic stainless steel, modelled using a Ramberg-Osgood relationship with Young's module of $E = 213\ GPa$, Poisson's ratio of $\nu = 0.285$, Yield strength and offset of $\sigma_o = 316\ MPa$ and $\alpha = 0.002$, respectively, and hardening exponent of $m = 8.45$ [34]. The boundary displacement is limited to only induce localised plasticity near the crack tip, as shown in Figure 3 (c).

For a commonly employed 5 MP camera setup, the validation setup equates to a step size of 20 pixels and a subset size of 41 pixels when using a 50% overlap between subsets. Considering a conservative limit of a DVC measurement accuracy of 0.1 voxels [35], this equates to a displacement accuracy of $5 \cdot 10^{-5}$ *mm*. For the applied BC this equates to a 0.5 % displacement noise.

Three sources of outliers are considered, in addition to a rigid body displacement of $1/10^{th}$ of the nodal spacing and rotation of 2º or 0.0349 *rad* (rigid-body displacement and rotation are seen as inherent attributes of DIC and DVC displacement measurements which should not result in any outlier removal). Sources of outliers are; i) Gaussian random noise equivalent to the displacement measurement accuracy; ii) smearing across the crack flanks using a Gaussian low bandpass filter equivalent to two subset sizes (i.e. four data points); and iii) the inclusion of an artefact that causes displacement amplitude ten times the displacement measurement accuracy with a diameter of two subset sizes (i.e. four data points).

Figure 4 shows the input displacement data, the respective outlier removal, and the identified outliers given in each column, respectively, when using a Grubbs filter. Figure 4 (a) shows the FE commutated displacement data without the addition to the artificial nose as the input data‡. The algorithm did not identify any outliers, including any localised plasticity ahead of the crack tip. Figure 4 (b) shows the FE commutated displacement data with the addition of the above-mentioned random Gaussian, subset smearing and artefact noise, visible by the uneven contour lines, smearing near the crack flanks and the artefact in the top right quadrant respectively. The algorithm required one iteration to identify, remove and replace 401 of 10150 (4 %) datapoints that are positioned next to the crack flanks and artefact region.

The outlier removal is best represented with the aid of Figure 5 and Figure 6, which show the histogram plots of the displacement noise and internal force vectors, respectively. Displacement noise values are computed by subtracting the FE computed from the added displacement noise fields shown in Figure 4 (a) and (b).

---

‡ A small amount ($5 \cdot 10^{-6}$ mm) of Gaussian noise floor was added to the FE data for numerical stability in the identification of outliers.

Figure 5 (a) highlights the nature of the displacement noise, in that the Gaussian noise results in a narrow symmetrical spread, the simulated subset smearing result in outliers with a wide symmetrical speed, and the artefact results in positively skewed spread due to the way the artefact noise was added. The variance and bias for the displacement field are $4.23 \cdot 10^{-4}$ and $3.24 \cdot 10^{-6}$ *mm*, respectively. The force vectors which are shown in Figure 6 (a) follow a near-identical trend and are seen as a direct representation of the displacement noise. The variance and bias for the force vectors are $2.66 \cdot 10^{-2}$ and $8.18 \cdot 10^{-3}$ *N*, respectively. Using the Grubbs filter, the force outliers are identified and set to zero. The resultant force distribution plot in Figure 6 (b) shows a narrow symmetrical spread that mostly contains contributions from the addition of Gaussian noise. The variance and bias after outlier removal for the force vectors are $6.88 \cdot 10^{-4}$ and near-zero[§] *mm*, respectively. The resultant displacement noise distribution plot is shown in Figure 5 (b) with no visible outliers. The variance and bias for the displacement field are $2.12 \cdot 10^{-6}$ and $7.64 \cdot 10^{-5}$ *mm*, respectively. The data shows that smearing and artefact contributions were removed, and that random Gaussian noise resulted in limited outlier removal. This is visible in Figure 4 (b) where the identified and replaced outliers are shown, which link with respective displacement field.

Similar to Figure 6, Figure 7 shows the displacement distribution plot using a median filter, setting $MAD \leq 3$. The variance and bias for the displacement field are $1.11 \cdot 10^{-6}$ and $3.32 \cdot 10^{-5}$ *mm*, respectively. While the Grubbs filter only required one iteration, the median filter took eight iterations removing 1643 of 10150 (16 %) data points. This is due to the way the convergence criteria are defined, where C2 is calculated as a change in outlier removal with respect to the input bias. Since a median filter will keep removing data points at a rate defined by MAD, a change in θ will occur until the force distribution becomes near symmetrical. This is easily seen when comparing Figure 5 (b) and Figure 7 (a). As such, a median filter can result in the smoothing of data. This can be seen in Figure 7 (b), whereby the filter started removing the imposed Gaussian noise.

To demonstrate the algorithm's independence in choice of elastic constants, the force value distribution plot is shown in Figure 8 for the choice in E and v. We note that both the choice

---

[§] Near-zero values are equal or less than E_{min}.

in E and v results in a change of the spread, albeit quite subtle for the choice in v, obtaining both a bias of near-zero. The reason for this is that the choice in E will only affect the respective force value and therefore not the nature of its statistical distribution, which forms the basis of the outlier detection. Similarly, the choice in v will affect the respective force value, however, equally in opposite directions, therefore again maintaining the nature of its statistical distribution.

Although the approach assumes a linear-elastic material model, localised non-linear regions remain unaffected by the filter due to the invariance to the choice in E and v. This remains only true if non-linearity remains smooth with low gradients such as the validation problem presented here. Large displacement deviations due to highly localised non-linear deformations will result in substantial force vectors that are identified as outliers. As such, care should be taken with regards to the sensitivity of the outlier removal algorithm and non-linear deformations.

Considering the reported accuracy of DIC of 0.01 in-plane and 0.05 pixels out-of-plane, and DVC of 0.1 voxels and the expect normally distributed variance noise in the computation of displacements, the algorithm should robustly remove bias contributions and maintain the inherent variance in the system. This is demonstrated in the following section.

4 Implementation on experimentally obtained DIC and DVC displacement fields

The experimental implementation uses two studies: (i) a Stereo-DIC computed displacement fields of a PMMA (Polymethyl methacrylate) Arcan specimen geometry, and (ii) DVC computed displacement fields of a Magnesium alloy (WE43) slanted single edge notched specimen. Both specimen geometries present a crack (discontinuity) loaded in mixed-mode, resulting in a complex crack tip stress field. Displacement fields were computed using a commercial software package DaVis (LaVision, Göttingen, Germany). While best practices were undertaken in the experimental setup to obtain low noise displacements fields, the data contains some form of variance and bias noise due to the inherent sensitivity of the setup and subset smearing across the discontinuity.

4.1 Stereo-DIC computed displacement fields

The Arcan setup comprises of a butterfly-shaped specimen that is clamped on opposite ends using fixtures that can rotate through different loading angles (of 15˚) including an out-of-plane offset. This allows for mixed-mode type loading in pure mode I and II, and mixed-mode I/II/III. The authors have previously presented the experiential setup and technique, and details can be found here [1].

Clear cast single-edge crack PMMA specimens were laser-cut from 6 mm sheets. Sharp pre-cracks were induced from the tip of a starter notch (15 mm) to a total length of 20 ± 1 mm using a razor blade. The specimen was loaded in mixed-mode at a loading angle of 30˚ to the pre-crack crack plane and an out-of-plane offset of 3 mm. A speckle pattern was applied using matt water-based spray paint, consisting of a white base coat and black speckles of 0.13 – 0.63 mm in size. Loading was undertaken using a Criterion Model 44 machine (MTS, Minnesota, USA) with a 30kN load cell at a crosshead displacement rate of 0.25mm/min. Images were captured using a StrainMaster (LaVision, Göttingen, Germany) DIC system. Table 2 summarises the key DIC hardware elements involved in this study.

Displacement fields were computed using DaVis 8.4 correlation software with key processing parameters highlighted in Table 3. Self-correlated tests, computed according to iDICs guidelines, resulted in an in-plane and out-of-plane noise floor value of 0.21 and 0.36 μm respectively, and an average rigid-body-motion error of 0.31 μm for a displacement of 1 mm. The DIC datasets resulted in 45 × 33 displacement data points.

The experimental input and outlier removed displacement fields are shown in Figure 9 for u_1, u_2 (in-plane) and u_3 (out-of-plane) as (a), (b) and (c), respectively. The force vector distribution is shown in Figure 10 (a) and the identified and replaced datapoint in (b). The outlier removal used a Grubbs filter with $k \leq 0.05$, $lim_{C1} = 1 \cdot 10^{-10}$, $lim_{C2} = 1 \cdot 10^{-2}$ and $lim_{C3} = 10$. 285 of 1421 data points (20.0 %) were replaced over two iterations, resulting in the replacement of ~ 10 % of data points per iteration.

Similar to the validation problem presented in Section 3, the outlier removal was mostly near the crack flanks due to the subset smearing across the crack flanks. Also identified were regions near the upper-end specimen region. This is likely to be due to specimen edge effects and how

boundary conditions are treated in the proposed outlier removal. Displacements on the boundary are extrapolated in the same way outliers are replaced. This may, if a more extensive region is replaced, result in some form of smoothing.

4.2 DVC computed displacement fields

The slanted SENT setup comprised a specimen geometry that is rectangular in cross-section with dimensions 10 × 20 mm over a 50 mm gauge region. The specimen ends are loaded using an in-situ X-CT fixture, whereby the top end remained fixed, and the bottom end is displaced in shear using a translation stage with an accuracy of 0.01 mm. A notch that is 30˚ to each axis was machined using wire–electrode discharge machining (wire-EDM) with a 0.3-mm diameter wire. The authors have previously presented the experiential setup and technique, and details can be found here [36].

WE43 contains 4-wt.% Yt and 3-wt.% Nd (balance Mg) to produce a good speckle contrast from X-CT reconstructions due to the attenuation variations between the Magnesium bulk material and precipitates that are richer in rare earth elements [5, 37]. The material is therefore well suited for DVC [38] as precipitates produce speckle features in the order of ~ 80 μm.

Tomographs were obtained using Stellenbosch University's X-CT scanner facility using a General Electric Phoenix VTomeX L240 microCT scanner with a 2 048 × 2 048 pixel detector with a 16-bit depth [39]. Optimised parameters were selected according to the guidelines set out in [40]. X-ray settings included 220 kV and 200 μA and copper beam filtration of 1.5 mm, with a voxel size set to 15 μm. Image acquisition time was 500 ms per image, and images were recorded in 2,000 rotation steps during a full 360˚ rotation of the specimen. At each step, the first image was discarded, and the next three images averaged to provide high image quality. Detector shift was activated to minimise ring artefacts, and automatic scan optimiser was activated to eliminate artefacts due to possible specimen movement or X-ray spot drift. Reconstruction was performed in the system supplied Datos reconstruction software. A summary of all tomography settings is provided in Table 4.

Displacement fields were computed using DaVis 8.3 correlation software with key processing parameters highlighted in Table 5. Image correlation used an initial subset size of 200 and a final subset size of 80 voxels. Self-correlated tests resulted in a noise floor value of 0.36 μm by

correlating the two identically loaded datasets. A rigid body displacement tests revealed an experimental accuracy of 1.4 μm (~ 0.1 voxels). The DVC datasets resulted in 74 × 44 × 60 displacement data points.

The experimental input and outlier removed displacement fields for the mid slice (in X_3, as indicated in Figure 11 (a)) are shown in (b), (c) and (d) for u_1, u_2 (in-plane) and u_3 (out-of-plane) respectively. The force vector distribution is shown in Figure 12 (a) and (b) for a Grubbs and median filter, respectively. The Grubbs filter (a), with $k \leq 0.05$, $lim_{C1} = 1 \cdot 10^{-10}$, $lim_{C2} = 1 \cdot 10^{-2}$ and $lim_{C3} = 10$, required two iterations replacing a total of 1913 of 109831 (1.74 %) data points, resulting in the replacement of ~ 0.87 % of data points per iteration. The median filter, with $MAD \leq 1$, $lim_{C1} = 1 \cdot 10^{-10}$, $lim_{C2} = 1 \cdot 10^{-2}$ and $lim_{C3} = 10$, required five iterations replacing a total of 74983 of 109831 (68.3 %) data points, resulting in the replacement of ~ 13.7 % of data points per iteration.

Although not shown in Figure 11 (b), the Grubbs filter did not significantly improve the displacement field and only removed data near the specimen edges where the X-CT contrast would have been low and therefore resulted in poor DVC correlation. Using a severe $MAD \leq 1$ resulted in significant data removal and smoothing. Nonetheless the nature of the complex displacement field is maintained, even near the notch geometry.

4.3 Discussion

The proposed FE-based outlier removal approach was shown to be robust in identifying and replacing outliers in Stereo-DIC and DVC computed displacement data. The basis of the approach is that the force vector data is used to filter and replace outliers. The advantage lies in that the force vector data should be normally distributed allowing for more straightforward outlier detection by using either a Grubbs or median filter. Other statistical outlier filters exist that may provide additional functionality. For example, a generalised extreme studentised deviate test for outliers, an iterative method that is similar to a Grubbs filter can perform better when multiple outliers are masking each other. Their complexity, however, does not necessarily warrant their application.

The choice in a Grubbs or median filter lies in the requirement for data smoothing; if only outliers are to be removed (as for the Stereo-DIC displacement data), a Grubbs filter offers the

advantage of maintaining the underlying variance level, whereas a median filter can be set to replace a significant amount of data points thereby smoothing data (DVC displacement data). A median filter allows for more control in data replacement per iteration by setting either a conservative or severe MAD.

Outlier detection is dependent on the statistical distribution of the force vector data, where a bias error would result in a shift from a non-zero mean and conversely, variance errors would affect the spread of the distribution. Therefore, a large scale subtle underlying bias may not be detectable using a Grubbs or median filter, as this would entail an overall shift in the distribution of the force vector data. Conversely, a single biased outlier may remain undetected if within the distribution of the variance error. The strength in the proposed outlier removal approach lies in identifying regions that have been tracked incorrectly, such as subset smearing across discontinuities, or ring artefacts in DVC data, in the overall accurately computed displacement field.

A further limitation of the approach is that a linear-elastic material model forms the basis of the FE framework. Although this does not affect localised and limited plastic deformation (as discussed in Section 3), materials that are exhibiting more complex behaviour, for example, anisotropy, may not be amenable to the approach. Moreover, noncontinuous structures, such as quasi-brittle materials [41, 42] and scaffolding or bone [43], will not necessarily work as a continuum is assumed.

5 Conclusions

This work proposed an FE-based outlier filter to identify and replace displacement outliers from 2D-DIC, Stereo-DIC and DVC displacement data. The approach uses reaction force vectors as an error estimator, whereby force vectors are filtered and replaced using a FE framework. It is shown that the outlier filter is robust in identifying outliers due to the nature of the force vector distribution, which can be seen to be representative of the variance and bias in the displacement data. The effectiveness of the outlier filter is tested using an idealised single edge notched example. It is shown through this example that classical random noise related to DIC or DVC accuracy is maintained and outliers contributing to displacement bias are removed. Experimentally, the outlier filter was found to be effective in the elimination of typical DIC and DVC artefacts. Moreover, the choice of filter allows for a choice in outlier removal and data smoothing.

Acknowledgments

The authors acknowledge the Stereo-DIC and DVC data and contributions from Matthew Molteno, and the X-CT reconstructions undertaken by the Central Analytical Facility at the Stellenbosch University.

Funding

This work is based on the research supported in part by the National Research Foundation of South Africa for the grant, Unique Grant Nos. 87955 and 106932.

Conflicts of Interest

The authors have no conflicts of interest to declare that are relevant to the content of this article.

References

1. Molteno MR, Becker TH (2015) Mode I-III decomposition of the j-integral from DIC displacement data. Strain 51:492–503. https://doi.org/10.1111/str.12166
2. Yoneyama S, Arikawa S, Kusayanagi S, Hazumi K (2014) Evaluating J-integral from displacement fields measured by digital image correlation. Strain 50:147–160. https://doi.org/10.1111/str.12074
3. Rannou J, Limodin N, Réthoré J, et al (2010) Three dimensional experimental and numerical multiscale analysis of a fatigue crack. Comput Methods Appl Mech Eng 199:1307–1325. https://doi.org/10.1016/j.cma.2009.09.013
4. Mostafavi M, Vertyagina Y, Reinhard C, et al (2014) 3D Studies of damage by combined X-ray tomography and digital volume correlation. In: 20th European Conference on Fracture. pp 1554–1559
5. Marrow TJ, Mostafavi M, Hashimoto T, Thompson GE (2014) A quantitative three-dimensional in situ study of a short fatigue crack in a magnesium alloy. Int J Fatigue 66:183–193. https://doi.org/10.1016/j.ijfatigue.2014.04.003
6. Fagerholt E, Borvik T, Hopperstad OS (2013) Measuring discontinuous displacement fields in cracked specimens using digital image correlation with mesh adaptation and crack-path optimization. Opt Lasers Eng 51:299–310. https://doi.org/10.1016/j.optlaseng.2012.09.010
7. Friedman LH, Vaudin MD, Stranick SJ, et al (2016) Assessing strain mapping by electron backscatter diffraction and confocal Raman microscopy using wedge-indented Si. Ultramicroscopy 163:75–86. https://doi.org/10.1016/j.ultramic.2016.02.001
8. Barhli SM, Saucedo Mora L, Simpson C, et al (2016) Obtaining the J-integral by diffraction-based crack-field strain mapping. In: Procedia Structural Integrity. Elsevier B.V., pp 2519–2526
9. Wattrisse B, Chrysochoos A, Muracciole JM, Némoz-Gaillard M (2001) Analysis of strain localization during tensile tests by digital image correlation. Exp Mech 41:29–39. https://doi.org/10.1007/BF02323101
10. Pan B (2018) Digital image correlation for surface deformation measurement: Historical developments, recent advances and future goals. Meas. Sci. Technol. 29:082001

11. Zou X, Li K, Pan B (2020) The Effect of Low-pass Pre-filtering on Subvoxel Registration Algorithms in Digital Volume Correlation: A revisited study. Meas Sci Rev 20:202–209. https://doi.org/10.2478/msr-2020-0025
12. Baldoni J, Lionello G, Zama F, Cristofolini L (2016) Comparison of different filtering strategies to reduce noise in strain measurement with digital image correlation. J Strain Anal Eng Des 51:416–430. https://doi.org/10.1177/0309324716646690
13. Morton J, Post D, Han B, Tsai MY (1990) A localized hybrid method of stress analysis: A combination of moir?? interferometry and FEM. Exp Mech 30:195–200. https://doi.org/10.1007/BF02410248
14. Yoneyama S (2011) Smoothing measured displacements and computing strains utilising finite element method. Strain 47:258–266. https://doi.org/10.1111/j.1475-1305.2010.00765.x
15. Yoneyama S, Arikawa S, Kurosu Y (2016) Evaluating thermal stresses and strains from measured displacements using an experimental-numerical hybrid method. In: Conference Proceedings of the Society for Experimental Mechanics Series. Springer, Cham, pp 103–110
16. Becker TH, Mostafavi M, Tait RB, Marrow TJ (2012) An approach to calculate the J -integral by digital image correlation displacement field measurement. Fatigue Fract Eng Mater Struct 35:971–984. https://doi.org/10.1111/j.1460-2695.2012.01685.x
17. Sutton MA, Turner JL, Bruck HA, Chae TA (1991) Full-field representation of discretely sampled surface deformation for displacement and strain analysis. Exp Mech 31:168–177. https://doi.org/10.1007/BF02327571
18. Nishioka T, Kurio K, Nakabayashi H (2000) An intelligent hybrid method to automatically detect and eliminate experimental measurement errors for linear elastic deformation fields. Exp Mech 40:170–179. https://doi.org/10.1007/BF02325043
19. Nishioka T, Ikekita H, Tamai K (1997) A variational principle for minimizing experimental measurement errors and its application to a hybrid experimental-numerical method. Comput Mech 20:101–108. https://doi.org/10.1007/s004660050224
20. Fujikawa M (2005) Modified Intelligent Hybrid Technique Reducing Experimental Error over the Entire Target Area. Exp Mech 45:541–549. https://doi.org/10.1177/0014485105059558
21. Sutton MA, Turner JL, Bruck HA, Chae TA (1991) Full-field representation of discretely sampled surface deformation for displacement and strain analysis. Exp Mech 31:168–177. https://doi.org/10.1007/BF02327571
22. Bendsøe MP (1989) Optimal shape design as a material distribution problem. Struct Optim 1:193–202. https://doi.org/10.1007/BF01650949
23. Markus Hegland, Stephen Roberts and IA (1997) Finite element thin plate splines for data mining applications. Maths 289–296
24. Garcia D (2010) Robust smoothing of gridded data in one and higher dimensions with missing values. Comput Stat Data Anal 54:1167–1178. https://doi.org/10.1016/j.csda.2009.09.020
25. Bigger R, Blaysat B, Boo C, et al (2018) A Good Practices Guide for Digital Image Correlation. Int Digit Image Correl Soc 94. https://doi.org/10.32720/idics/gpg.ed1
26. Transactions ECS, Society TE (2010) Preliminary Evaluation of Digital Image Correlation for In-situ Observation of Low Temperature Atmospheric-Induced Chloride Stress Corrosion Cracking in Austenitic Stainless Steels A. Cook. 25:119–132
27. Atkinson D, Becker T (2020) A 117 Line 2D Digital Image Correlation Code Written in MATLAB. Remote Sens 12:2906. https://doi.org/10.3390/rs12182906
28. Liu K, Tovar A (2014) An efficient 3D topology optimization code written in Matlab. Struct Multidiscip Optim 50:1175–1196. https://doi.org/10.1007/s00158-014-1107-x

29. Cinar AF, Barhli SM, Hollis D, et al (2017) An autonomous surface discontinuity detection and quantification method by digital image correlation and phase congruency. Opt Lasers Eng 96:94–106. https://doi.org/10.1016/j.optlaseng.2017.04.010
30. Law J, Hampel FR, Ronchetti EM, et al (1986) Robust Statistics-The Approach Based on Influence Functions.
31. Grubbs FE (1950) Sample Criteria for Testing Outlying Observations. Ann Math Stat 21:27–58. https://doi.org/10.1214/aoms/1177729885
32. Barhli SM, Saucedo-Mora L, Jordan MSL, et al (2017) Synchrotron X-ray characterization of crack strain fields in polygranular graphite. Carbon N Y 124:357–371. https://doi.org/10.1016/j.carbon.2017.08.075
33. Becker TH, Marrow TTJ, Tait RRB, Mostafavi M (2011) Damage, crack growth and fracture characteristics of nuclear grade graphite using the Double Torsion technique. J Nucl Mater 414:32–43. https://doi.org/10.1016/j.jnucmat.2011.04.058
34. Dowling N (2013) Mechanical Behavior of Materials: Engineering Methods for Deformation, Fracture, and Fatigue, Fourth Edi
35. LaVision (2014) Digital Volume Correlation (DVC)
36. Becker TH, Molteno MR, Marrow TJ (2020) Procedure for accurate calculation of the J-integral from digital volume correlation displacement data. Strain 56:1–18. https://doi.org/10.1111/str.12337
37. King A, Ludwig W, Herbig M, et al (2011) Three-dimensional in situ observations of short fatigue crack growth in magnesium. Acta Mater 59:6761–6771. https://doi.org/10.1016/j.actamat.2011.07.034
38. Mostafavi M, Collins DM, Cai B, et al (2015) Yield behavior beneath hardness indentations in ductile metals, measured by three-dimensional computed X-ray tomography and digital volume correlation. Acta Mater 82:468–482. https://doi.org/10.1016/j.actamat.2014.08.046
39. du Plessis A, le Roux SG, Guelpa A (2016) The CT Scanner Facility at Stellenbosch University: An open access X-ray computed tomography laboratory. Nucl Instruments Methods Phys Res Sect B Beam Interact with Mater Atoms 384:42–49. https://doi.org/10.1016/j.nimb.2016.08.005
40. du Plessis A, Broeckhoven C, Guelpa A, le Roux SG (2017) Laboratory X-ray micro-computed tomography: a user guideline for biological samples. Gigascience 6:1–11. https://doi.org/10.1093/gigascience/gix027
41. Hindley MP, Blaine DC, Groenwold A a., Becker TH (2015) Failure prediction of full-size reactor components from tensile specimen data on NBG-18 nuclear graphite. Nucl Eng Des 284:1–9. https://doi.org/10.1016/j.nucengdes.2014.12.011
42. Becker TH, Marrow T, Tait R, Mostafavi M (2010) Damage , Crack Growth and Fracture Characteristics of Nuclear Grade Graphite using the Double Torsion Technique. In: IYNC. Elsevier B.V., Cape Town, pp 274.1-274–16
43. Yan L, Cinar A, Ma S, et al (2020) A method for fracture toughness measurement in trabecular bone using computed tomography, image correlation and finite element methods. J Mech Behav Biomed Mater 109:103838. https://doi.org/10.1016/j.jmbbm.2020.103838

Table 1. Outlier removal algorithm.

Algorithm 1 Outlier detection and removal	
1	Define and pad **Ω**;
2	Set $\rho_l \leftarrow$ mask and compute $E_l(\rho_l)$ using Equation (1);
3	Compute $\boldsymbol{K}_l(E_l, v)$ using Equation (2), assemble $\boldsymbol{K}(\boldsymbol{K}_l)$ using Equation (3);
4	Set $\boldsymbol{u}_n \leftarrow$ experimental displacement field;
5	Set $\boldsymbol{f}_e \leftarrow 0$;
6	Initialise $i \leftarrow 0$, $flag = 0$;
7	Set C1, C2 and C3, using Equations (8), (9) and (10) ;
8	**while** $flag = 0$ **do**
9	Set $i \leftarrow i + 1$;
10	Compute $\boldsymbol{u}_e$ using Equation (6);
11	Compute $\boldsymbol{f}_n$ using Equation (5);
12	Identifying outliers in $\boldsymbol{f}_n$;
13	Compute $\theta^{(i)}$ using Equation (7)
14	**If** C1 is met **do**
	Set flag ← 1
15	**elseif** C2 is met **do**
	Set flag ← 2
16	**elseif** C3 is met **do**
	Set flag ← 3
	end if
17	Set $\boldsymbol{f_e} \leftarrow 0$ for outliers;
	end while
18	Remove padded array from **Ω**;

Table 2 - Hardware details for DIC setup.

Camera	LaVision Imager E-lite 12-bit, 5 MP CCD cameras
Image resolution	2 456 × 2 058 pixels^2
Lens	35 mm lenses
Aperture	f/1.8
Field of view	60 × 50 mm^2
Magnification factor	41 pixels/mm
Stereo angle	31 ˚
Stand-off distance	~ 400 mm
Image acquisition rate	1 Hz
Lighting	Pair of LaVision white linear units consisting of 12 LEDs each, 20 W, 6 500K colour temperature
Patterning technique	White base coat with corresponding black speckles applied via spray can.
Pattern feature size (average)	0.15 – 0.65 mm (6 – 25 pixels)

Table 3 - DIC analysis parameters.

Software	LaVision DaVis 8.4
Subset size	85 pixels (Gaussian-weighted)
Step size	20 pixels
Subset shape function	Affine
Matching criterion	Zero-normalised sum of squared differences (ZNSSD)
Interpolant	Bicubic spline
Region of interest (ROI)	40×30 mm^2 centred at the crack tip
Displacement noise floor	0.21 μm in-plane, 0.36 μm out-of-plane
Rigid body error (x direction)	0.31 μm

Table 4 - Hardware details for X-CT setup.

X-CT scanner	General Electric Phoenix VTomeX L240
Detector resolution	2048 × 2048
Rotation steps	0.18˚
Image acquisition time	500 ms
Reconstruction field of view	1260 x 1860 x 2024 voxels / 18.9 x 27.9 x 30.4 mm
Reconstruction bit depth	8 bit
Reconstruction voxel size	15 μm
Reconstruction software	Phoenix Datos X
Feature size	~ 80 μm

Table 5 - DVC analysis parameters.

Volume Correlation software	DaVis version 8.3
Subset size	80 voxels
Step size	20 voxels
Matching Criterion	Fast Fourier Transform
No of displacement vectors	44 x 74 x 60
Displacement smoothing	2^{nd} order polynomial over 5 data points
Displacement noise floor	0.36 µm
Rigid-body displacement noise	1.4 µm

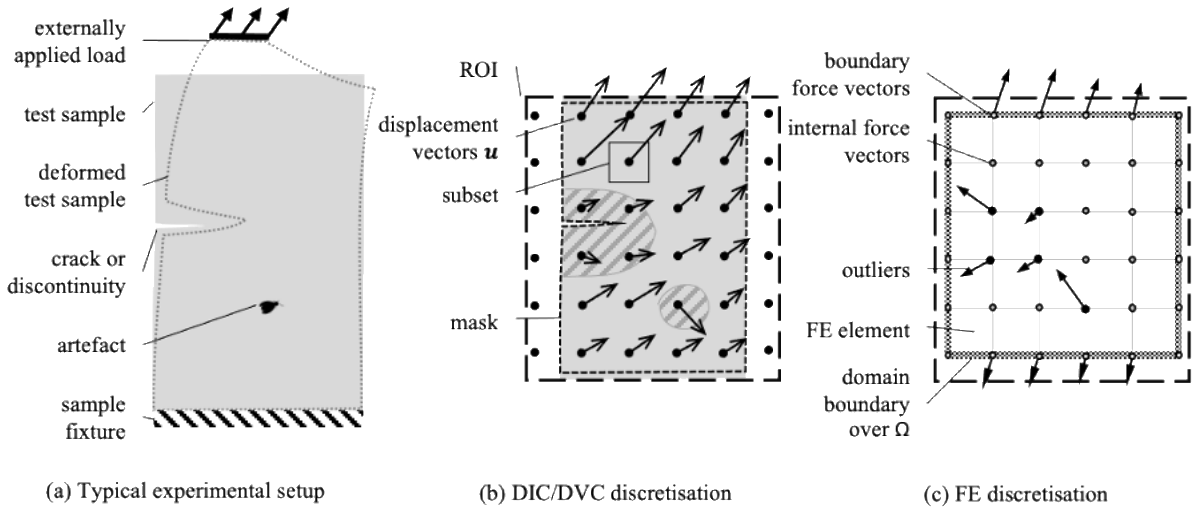

Figure 1. (a) Illustration of experimental loading of a test specimen. Shown is a discontinuity in the form of a crack and an artefact. (b) Acquisition of full-field displacement map using DIC or DVC and the definition of the mask. (c) FE discretisation showing forces at internal nodes and the boundary over domain Ω.

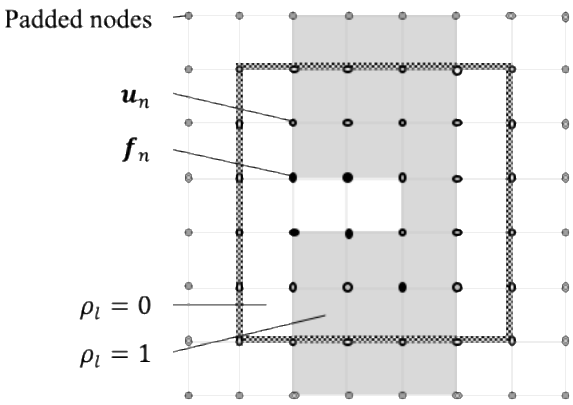

Figure 2. Nodal information over Ω.

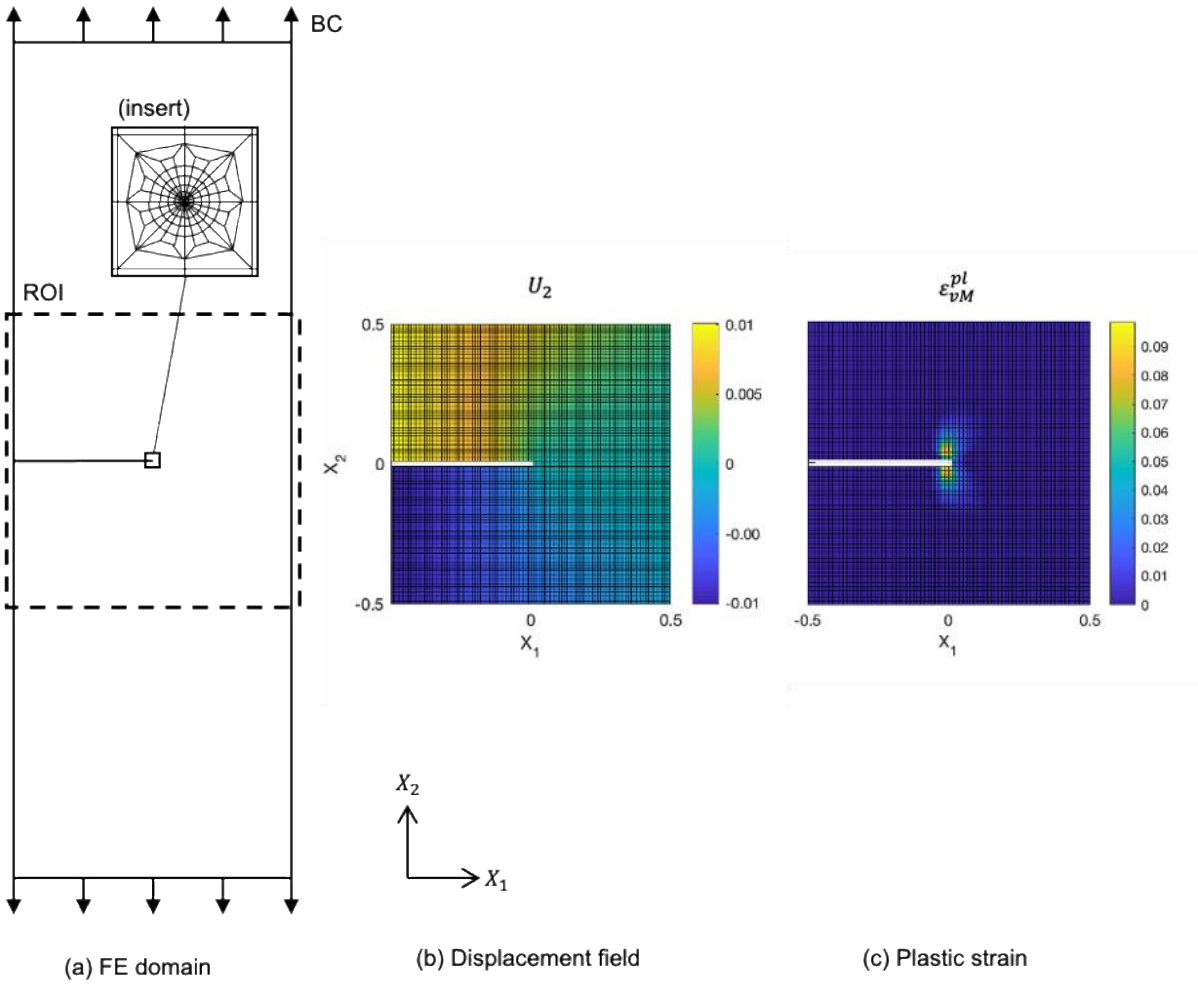

Figure 3. (a) FE model of validation setup. Insert showing notch tip mesh. (b) Equivalent DIC gridded displacement field of the central ROI. (c) Showing von Mises computed plastic strain, localised around the crack tip.

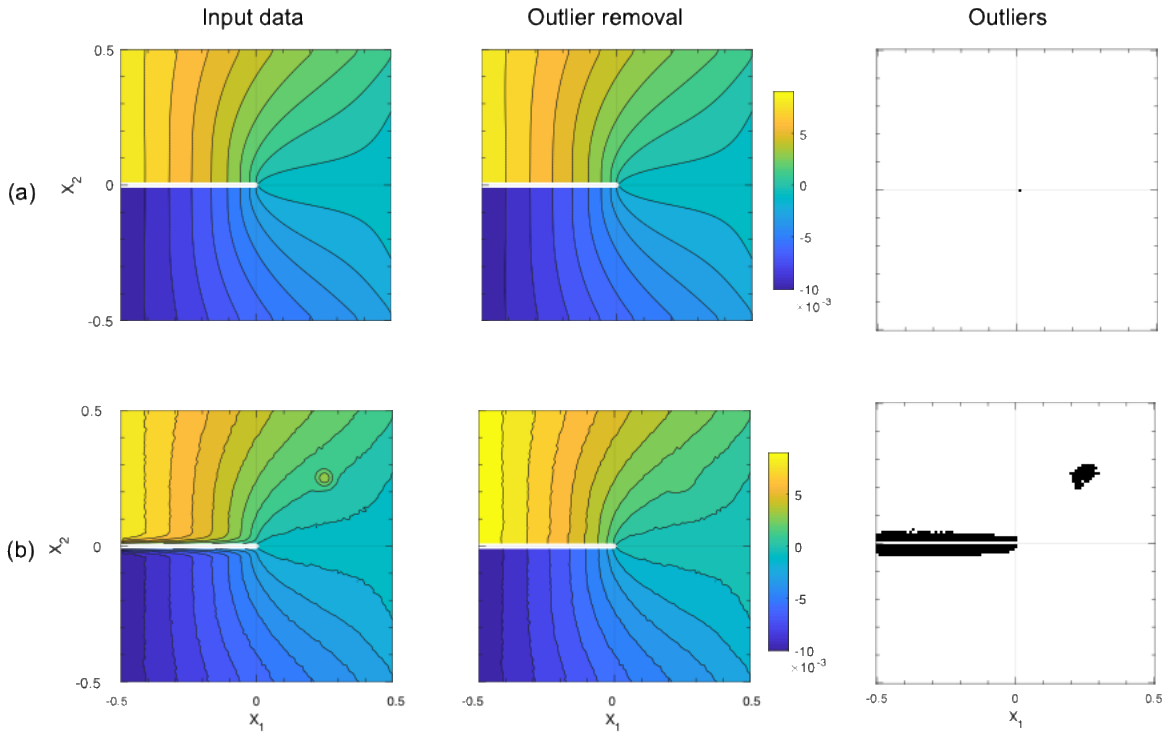

Figure 4. Input data, outlier removal and identified outliers for (a) the FE computed displacement data, and (b) added noise (random Gaussian, subset smearing and artefact) displacement data.

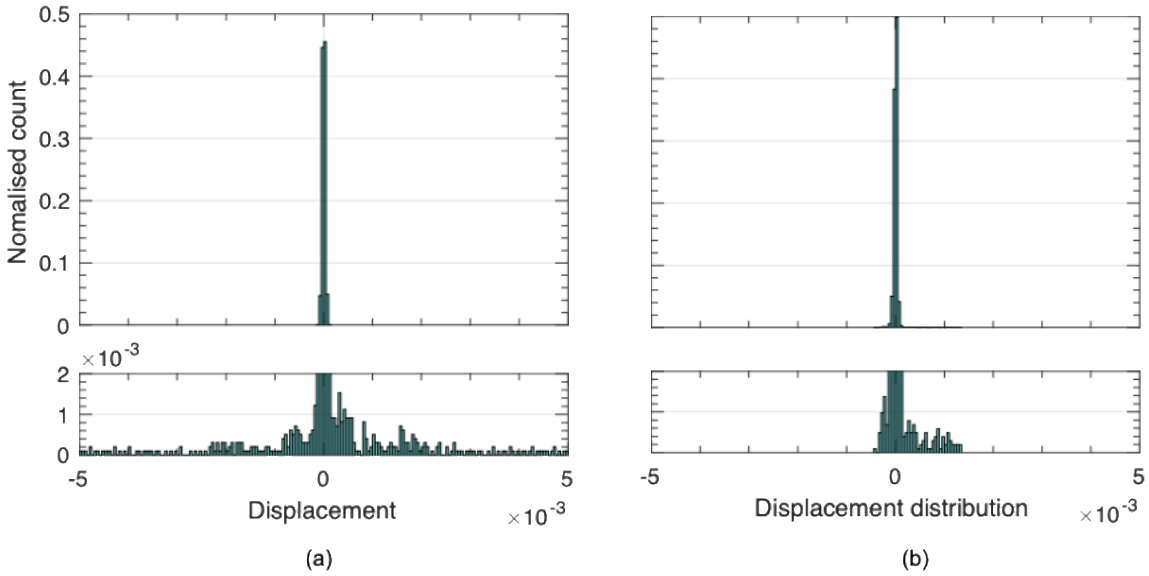

Figure 5. Displacement noise histogram in U_2 of (a) input data and (b) after outlier removal. The bottom graphs show a scaled section of the histogram to better highlight the distribution plot. The bin width is $5 \cdot 10^{-5}$ mm.

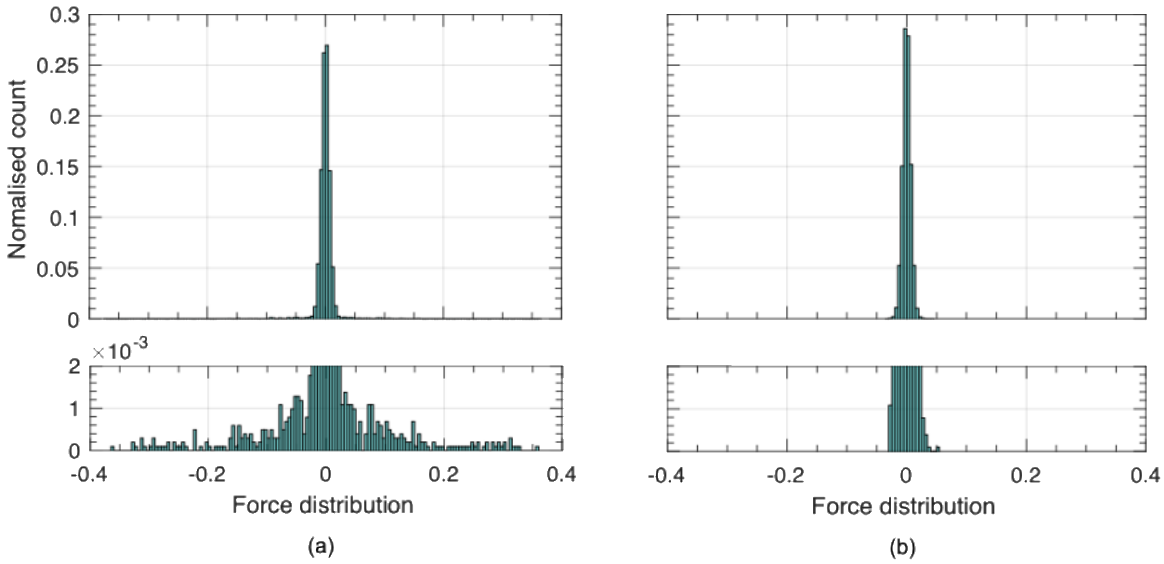

Figure 6. Force vector histogram in F_2 of (a) input data and (b) after outlier removal. The bottom graphs show a scaled section of the histogram to better highlight the distribution plot. The bin width is 5 · 10-3 N.

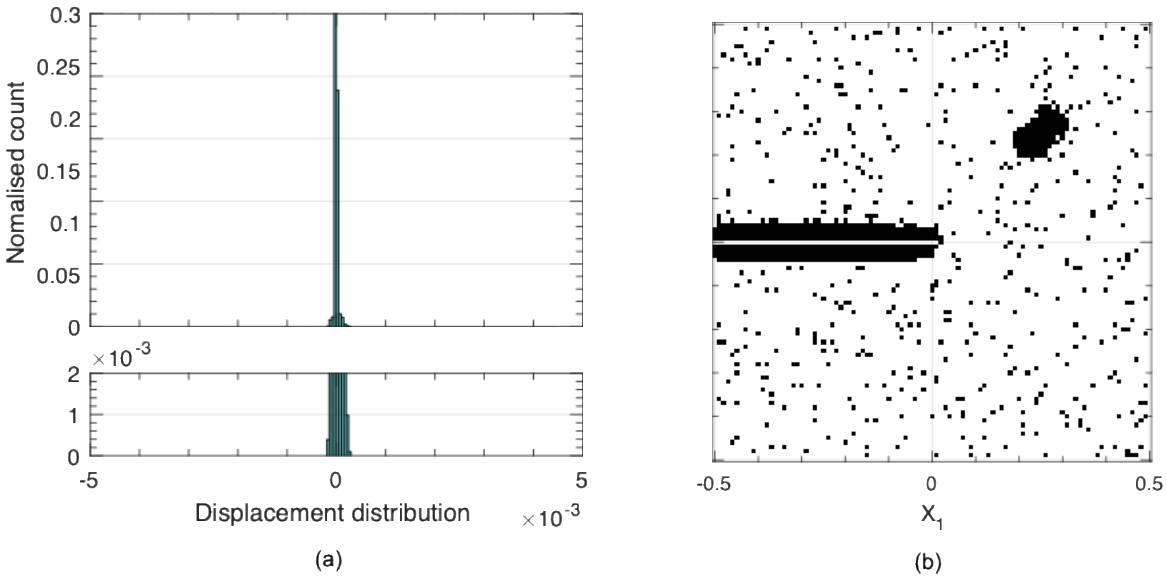

Figure 7. (a) Displacement vector histogram in U_2 after outlier removal, and (b) identified and replaced outliers.

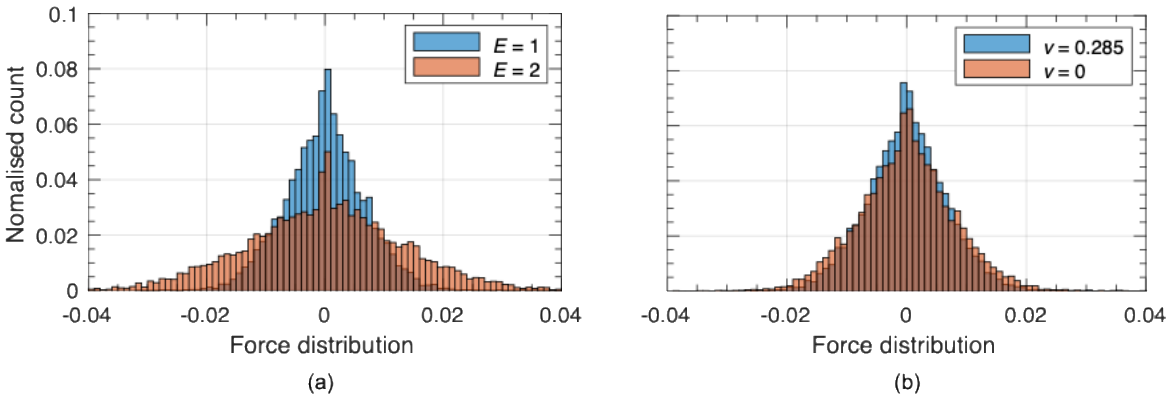

Figure 8. Force vector histogram in F_2 with respect to (a) choice of E and (b) v. The bin width is $5 \cdot 10^{-3}$ N.

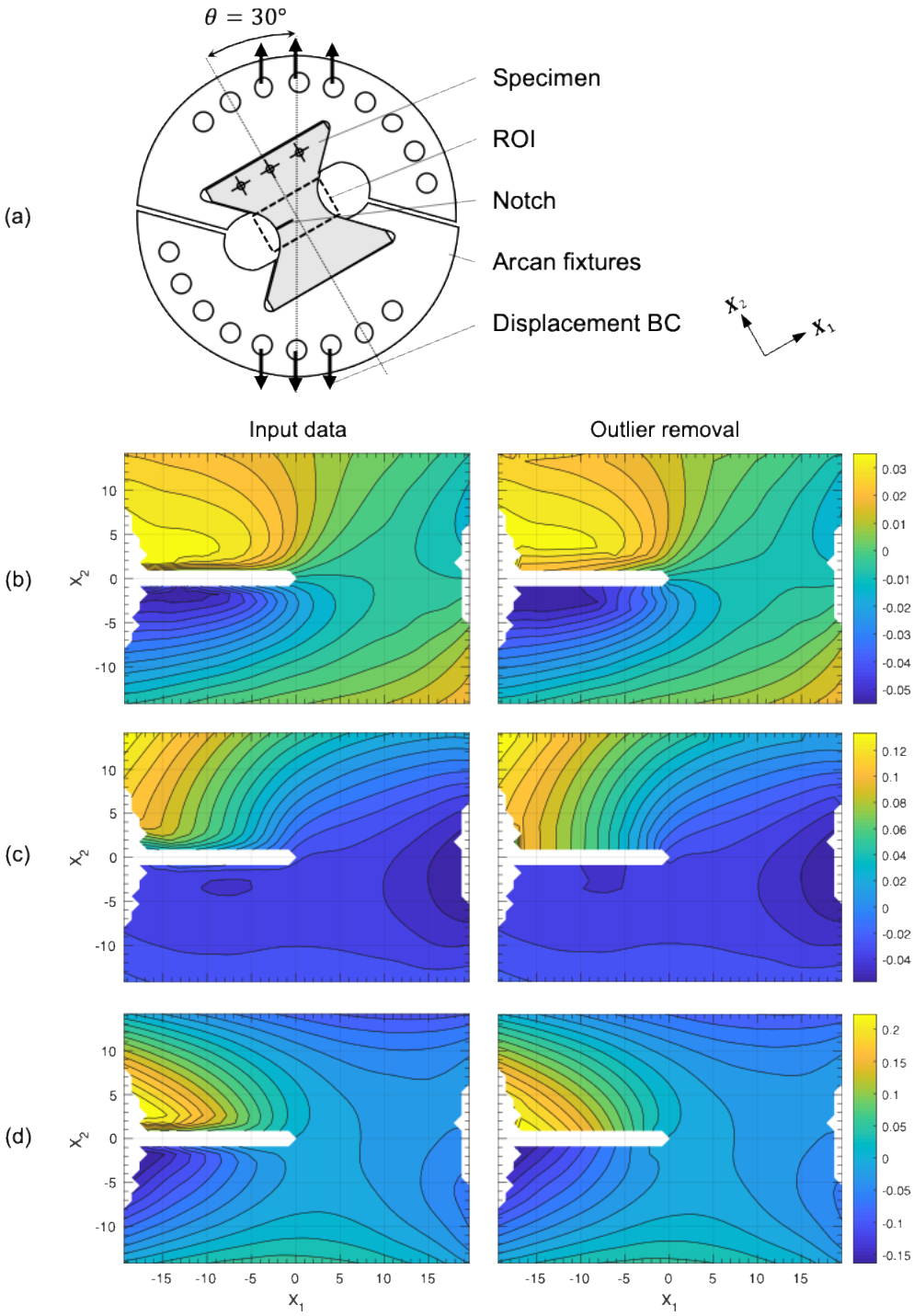

Figure 9. (a) Illustration of Arcan test setup, and Input data and Outlier removal over ROI showing displacement data in (b) u_1, (c) u_2 and (d) u_3.

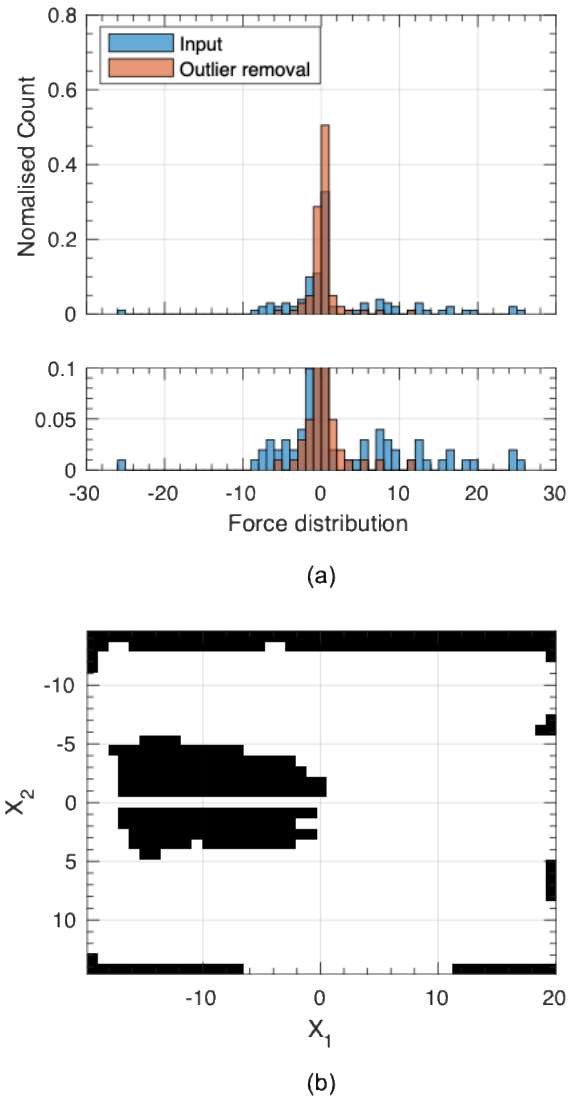

Figure 10. (a) Input data bias and variance is 5.80 and 38.5 N, respectively. Outlier removal data bias and variance is 5.53 and 11.6 N. (b) Identified and replaced outliers. The bin width is 1 N.

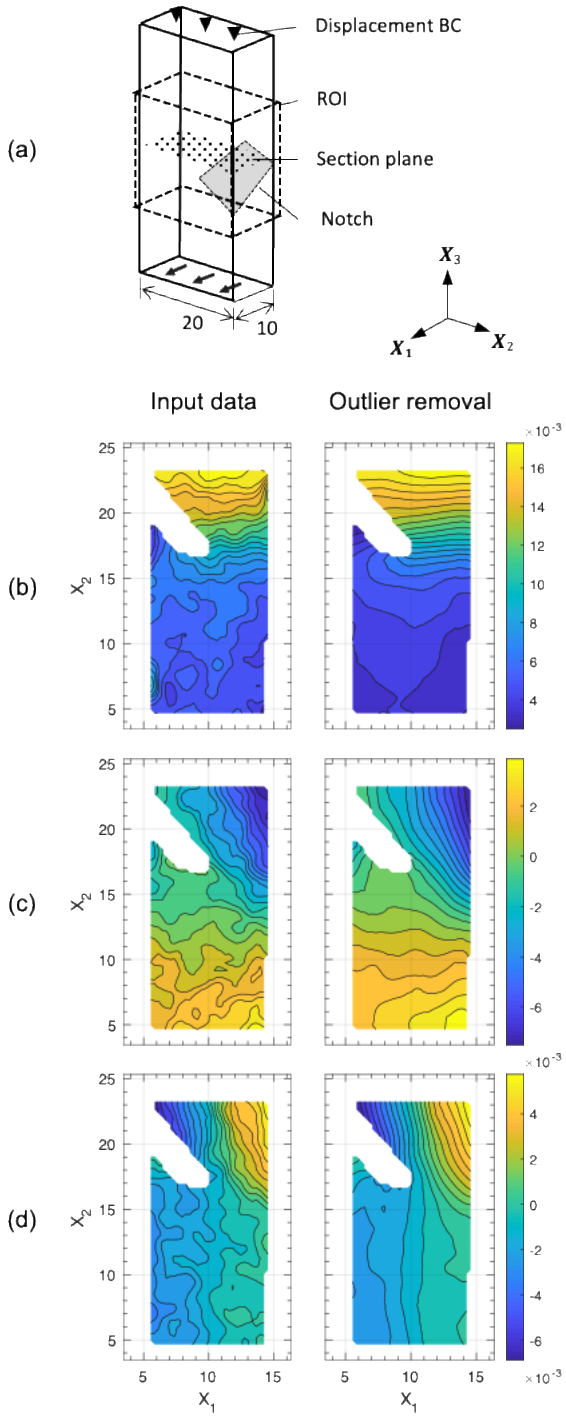

Figure 11. (a) Illustration of slated single edged notch test setup, and Input data and Outlier removal using median filter over ROI showing displacement data in (b) u_1, (c) u_2 and (d) u_3.

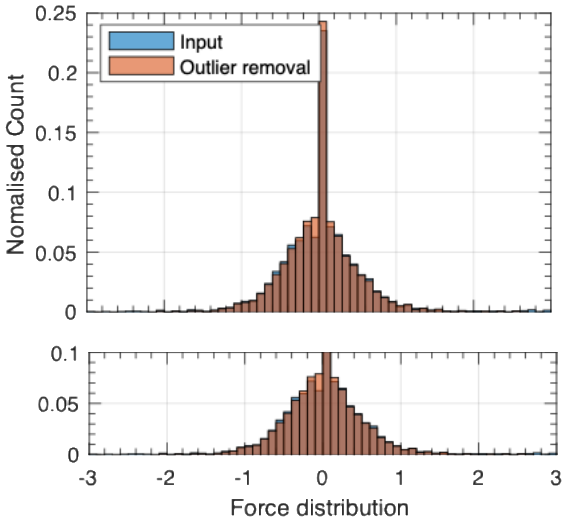

(a)

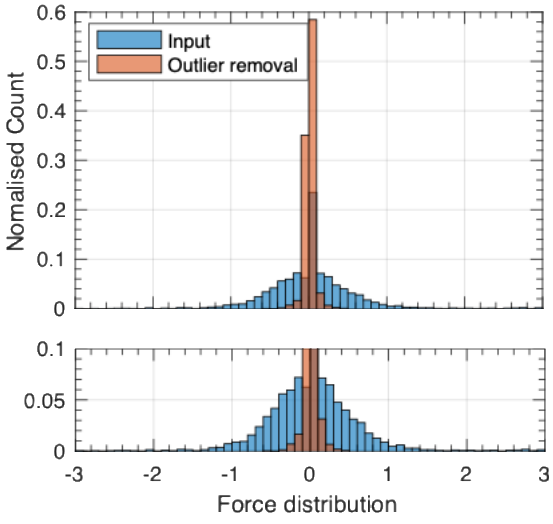

(b)

Figure 12. (a) Grubbs and (b) median filter. For (a) the input and output data bias and variance is $9.81 \cdot 10^{-1}$ *and* $8.89 \cdot 10^{-1}$*, and* $9.62 \cdot 10^{-1}$ *and* $6.13 \cdot 10^{-1}$*, respectively. For (b) the output data bias and variance is* $1.85 \cdot 10^{-1}$ *and* $1.55 \cdot 10^{-1}$*, respectively.*